Structural Engineering and Mechanics, *Vol. 58, No. 5 (2016) 799-823*
DOI: http://dx.doi.org/10.12989/sem.2016.58.5.799

Numerical simulation of reinforced concrete nuclear containment under extreme loads

Jorge Luis Palomino Tamayo[*1] and Armando Miguel Awruch[2a]

[1]*Center of Applied Mechanics and Computational (CEMACOM), Engineering School of Federal University of Rio Grande do Sul, Av. Osvaldo Aranha 99-3º Floor, 90035-190, Porto Alegre, RS, Brazil*
[2]*Department of Civil Engineering, Engineering School Federal University of Rio Grande do Sul, Av. Osvaldo Aranha 99-3º Floor, 90035-190, Porto Alegre, RS, Brazil*

(Received June 27, 2015, Revised February 6, 2016, Accepted March 2, 2016)

Abstract. A finite element model for the non-linear dynamic analysis of a reinforced concrete (RC) containment shell of a nuclear power plant subjected to extreme loads such as impact and earthquake is presented in this work. The impact is modeled by using an uncoupled approach in which a load function is applied at the impact zone. The earthquake load is modeled by prescribing ground accelerations at the base of the structure. The nuclear containment is discretized spatially by using 20-node brick finite elements. The concrete in compression is modeled by using a modified Drücker-Prager elasto-plastic constitutive law where strain rate effects are considered. Cracking of concrete is modeled by using a smeared cracking approach where the tension-stiffening effect is included via a strain-softening rule. A model based on fracture mechanics, using the concept of constant fracture energy release, is used to relate the strain softening effect to the element size in order to guaranty mesh independency in the numerical prediction. The reinforcing bars are represented by incorporated membrane elements with a von Mises elasto-plastic law. Two benchmarks are used to verify the numerical implementation of the present model. Results are presented graphically in terms of displacement histories and cracking patterns. Finally, the influence of the shear transfer model used for cracked concrete as well as the effect due to a base slab incorporation in the numerical modeling are analyzed.

Keywords: reinforced concrete structures (RC); finite element method (FEM); impact and seismic loads

1. Introduction

Containment shells are an important component of nuclear power plants and are normally constructed from reinforced concrete (RC). Because these structures are necessary for the production of nuclear energy, special consideration must be taken in their analysis and design. The nuclear containment structures provide biological and nuclear shielding to limit the radiation close to the atmosphere in cases of accidents. The nuclear containment structure is a double shell structure where the outer containment structure is made up of concrete to protect the inner

∗Corresponding author, Ph.D., E-mail: lpt.jorge@gmail.com
[a]Ph.D., E-mail: amawruch@ufrgs.br

http://www.techno-press.org/?journal=sem&subpage=8 ISSN: 1225-4568 (Print), 1598-6217 (Online)

containment from any external impact (Pandey *et al*. 2006, Pandey 2010, Sadique *et al*. 2015, Sayed *et al*. 2015). The vulnerability of these structures is an important aspect when they are constructed in seismic zones (Kamagata and Takewaki 2013) or when they are exposed to accidental or deliberate crash of aircrafts in zones with hectic air traffic (Sadique *et al*. 2015, Iqbal *et al*. 2012). While these structures are invariably designed to remain elastic under normal service conditions, they may suffer distress under the action of unforeseen extreme loads (Manjuprasad *et al*. 2001). In this work, a numerical model based on the finite element method is presented for the analysis of RC shells under aircraft impacts and seismic actions. For this purpose, 20-node brick finite elements are used to model the concrete walls of the containment while reinforcing steel bars are considered to be smeared within each finite element. Concrete cracking, nonlinearity of concrete in compression, yielding of the steel bars in tension and compression and strain rate effects are considered properly in the present material model. The RC model combines different features of some previous models proposed by other authors that makes it suitable and different for the analysis of the examples presented in this paper (see Tamayo *et al*. 2013a, b, Dias *et al*. 2015).

The numerical model is verified by analyzing the outer containment structure of the General Electric Mark-III nuclear reactor under impact and seismic loads. This containment structure has been previously studied by other researches (see e.g., Cervera 1986, Cervera *et al*. 1988, Liu 1985, Kukreja 2005, Abbas *et al*. 1996) using elasto-viscoplastic algorithms to perform stress integration. Generally, this structure has been analyzed with a coarse finite element mesh. In this work, a more refined finite element mesh is used and the solution phase of the nonlinear algorithm is optimized by using the PARDISO solver (Schenk and Gartner 2004), which is a thread-safe, high-performance and memory efficient package for solving large sparse symmetric linear systems of equations on shared-memory and distributed-memory multiprocessors. This package was incorporated in the present finite element code in order to take advantage of parallel computation by using OpenMP directives.

A parametric study is carried out in order to assess the importance of the shear retention model used for cracked concrete and the influence of a concrete base slab in the numerical model. Generally, the base slab is omitted in the model and the outer walls of the containment are considered to be clamped to the ground directly. The effect of these two last issues were investigated in the work of Hu and Liang (2000) for ultimate analysis of BWR Mark III RC containment subjected to internal static pressure, however they have not been addressed before for the Mark III outer containment under impact and seismic loads.

2. Finite element formulation and constitutive model for the brick element

The 20-node isoparametric quadratic brick element shown in Fig. 1 is used here to represent the concrete shell structure while the reinforcing steel bars are modeled using a smeared layer approach (mesh reinforcement is modeled as a membrane element). The displacement field within the element is defined in terms of the shape functions and displacement values at the nodes. Each nodal point has three degrees of freedom *u*, *v* and *w* along the Cartesian coordinates *x*, *y*, *z*, respectively. Therefore, for each element the displacement vector is expressed in the following manner

$$\boldsymbol{U} = \{u_1, v_1, w_1, u_2, v_2, w_2 \ldots\ldots\ldots u_{20}, v_{20}, w_{20}\} \tag{1}$$

The strain components vector, in terms of displacement components, is defined by

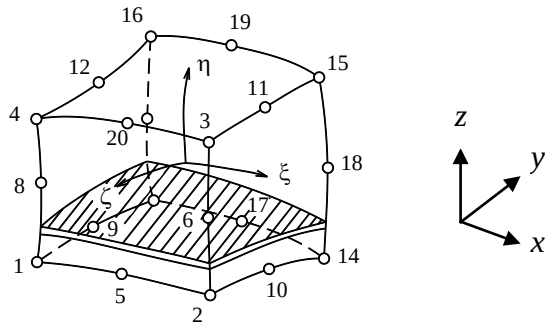

Fig. 1 Natural system: 20-node brick element

$$\boldsymbol{\varepsilon} = \begin{Bmatrix} \varepsilon_x \\ \varepsilon_y \\ \varepsilon_z \\ \gamma_{xy} \\ \gamma_{yz} \\ \gamma_{xz} \end{Bmatrix} = \sum_{k=1}^{20} \begin{bmatrix} \frac{\partial N_k}{\partial x} & 0 & 0 & \frac{\partial N_k}{\partial y} & 0 & \frac{\partial N_k}{\partial x} \\ 0 & \frac{\partial N_k}{\partial y} & 0 & \frac{\partial N_k}{\partial x} & \frac{\partial N_k}{\partial z} & 0 \\ 0 & 0 & \frac{\partial N_k}{\partial z} & 0 & \frac{\partial N_k}{\partial y} & \frac{\partial N_k}{\partial z} \end{bmatrix}^T \begin{Bmatrix} u_k \\ v_k \\ w_k \end{Bmatrix} \tag{2}$$

or

$$\boldsymbol{\varepsilon} = \boldsymbol{B}.\boldsymbol{U} \tag{3}$$

where N_k is the shape function of node k and $\boldsymbol{B}$ is the usual strain-displacement matrix. The stress and strain components are related by the following expression

$$\boldsymbol{\sigma} = \begin{bmatrix} \sigma_x & \sigma_y & \sigma_z & \tau_{xy} & \tau_{yz} & \tau_{xz} \end{bmatrix}^T = \boldsymbol{D}.\boldsymbol{\varepsilon} \tag{4}$$

where $\boldsymbol{D}$ is the material constitutive matrix in the global system. Equivalent nodal forces, at a given iteration i, are expressed in the following manner

$$\boldsymbol{P}^i = \int_V \boldsymbol{B}^T \boldsymbol{\sigma}^i \, d\Omega \tag{5}$$

while the stiffness matrix for a concrete element of volume Ω can be expressed as

$$\boldsymbol{K}^i = \int_V \boldsymbol{B}^T \boldsymbol{D}_{et}^i \boldsymbol{B} d\Omega \tag{6}$$

where $\boldsymbol{D}_{et}$ is the uncracked, cracked or elasto-plastic constitutive matrix for the concrete material and the elastic or elasto-plastic constitutive matrix for the steel reinforcement. A reduced integration rule of eight points is found to be suitable to diminish shear locking effect. Concrete in compression is modeled using the associated theory of plasticity (Tamayo *et al*. 2013a, b); a modified Drucker-Prager yield criterion (see Fig. 2(a)), which was proposed by Cervera (1986), is used in this work. Due to nonlinear hardening behavior, this yield criterion defines an initial yield surface at an effective stress equal to σ_0=0.3 f_c (which is the beginning of the plastic deformation, where f_c is the concrete compressive strength) and a limit surface separating a nonlinear state from

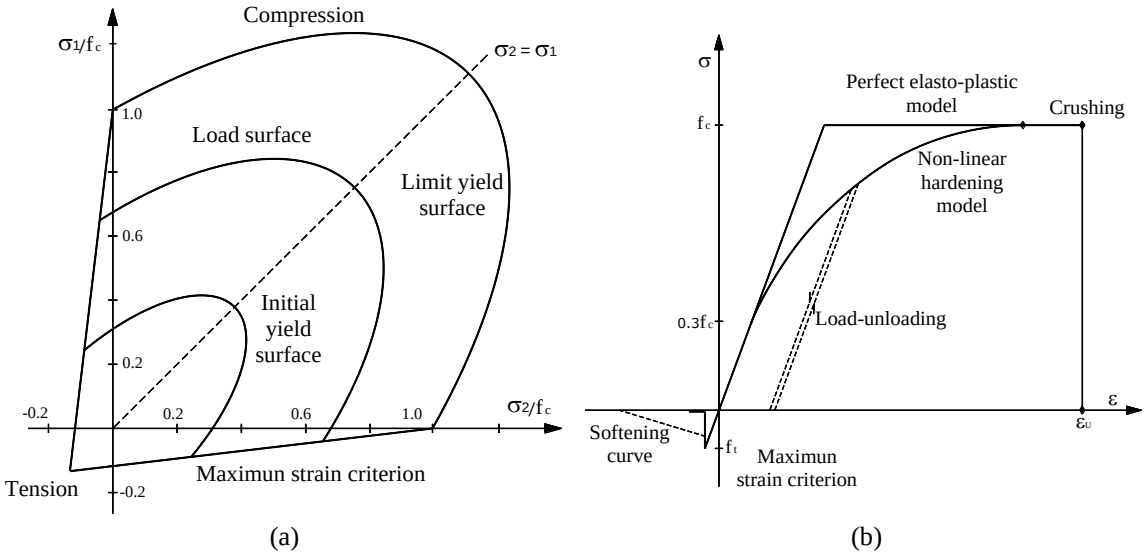

Fig. 2 Constitutive models for concrete: (a) Bi-axial representation (b) Uni-axial representation

a perfect elasto-plastic one, as it is shown in Fig. 2(b). The yield criterion is defined as

$$F(\boldsymbol{\sigma}) = cI_1 + \left\{c^2 I_1^2 + 3mJ_2\right\}^{1/2} = \sigma_o(\bar{\varepsilon}_p) \tag{7}$$

where I_1 and J_2 are the first and the deviatoric second stress invariants, respectively. In addition, σ_0 is the effective stress which depends on the effective plastic deformation $\bar{\varepsilon}_p$, being this last parameter defined in terms of the plastic work developed by the material. The constants c and m are evaluated from experimental test and are equal to 0.1775 and 1.355, respectively. The associated flow rule is defined as

$$d\varepsilon_{ij}^p = d\lambda \frac{\partial F(\sigma)}{\partial \sigma_{ij}} = \frac{\boldsymbol{g}^T \boldsymbol{D}_e}{H' + \boldsymbol{g}^T \boldsymbol{D}_e \boldsymbol{g}} d\boldsymbol{\varepsilon} \frac{\partial F(\sigma)}{\partial \sigma_{ij}} \tag{8}$$

with the flow vector given by

$$\boldsymbol{g}^T = \left[\frac{\partial F}{\partial \sigma_x} \quad \frac{\partial F}{\partial \sigma_y} \quad \frac{\partial F}{\partial \sigma_{xy}} \quad \frac{\partial F}{\partial \sigma_{xz}} \quad \frac{\partial F}{\partial \sigma_{yz}} \right] \tag{9}$$

In Eq. (8), $d\varepsilon$ contains the components of the total strain, $d\varepsilon_{ij}^p$ is a component of the plastic strain tensor, $\boldsymbol{D}_e$ is the elastic constitutive matrix and H' is the hardening parameter established as the slope of the one-dimensional curve which defines the hardening rule. This curve known as "Madrid parabola" (see Fig. 2(b)) is defined by the following expression

$$\sigma_y = H(\bar{\varepsilon}_p) = E_c \bar{\varepsilon}_p + \left(2E_c^2 \varepsilon_o \bar{\varepsilon}_p\right)^{1/2} \tag{10}$$

where E_c is the elastic modulus, ε_o represents the total strain at maximum compression stress f_c. The elasto-plastic constitutive relation is expressed in the following differential form

$$d\boldsymbol{\sigma} = \boldsymbol{D}_{et} d\boldsymbol{\varepsilon} = \left\{ \boldsymbol{D}_e - \frac{\boldsymbol{D}_e \boldsymbol{g}.\boldsymbol{g}^T \boldsymbol{D}_e}{H' + \boldsymbol{g}^T \boldsymbol{D}_e \boldsymbol{g}} \right\} d\boldsymbol{\varepsilon} \tag{11}$$

where $\boldsymbol{D}_{et}$ is the elasto-plastic constitutive matrix. Finally, the crushing condition is given by

$$cI_1' + \left\{ c^2 I_1'^2 + 3mJ_2' \right\}^{1/2} = \varepsilon_u \tag{12}$$

where I_1' and J_2' are the first and the deviatoric second strain invariants, respectively and ε_u represents the ultimate deformation extrapolated from experimental tests (it is taken here as 0.0035). Otherwise, earlier developments and studies (Liu 1985) suggest that a concrete model intended for transient analysis should be rate and history dependent. To describe rate effects, the constitutive law, which was first introduced in Eq. (7), can be rewritten as

$$\sigma_{od} = \sigma_o(\bar{\varepsilon}_p) \left\{ 1 + 0.0279 \left(\frac{\dot{\varepsilon}}{10^{-5}} \right)^{0.3302} \right\} \tag{13}$$

in which σ_{od} is now a yield function both of the strain history and the current strain rate $\dot{\varepsilon}$. The reader is referred to the works of Tamayo *et al*. (2013a, b) for more details about this consideration. Otherwise, because the cracking tensile strain of concrete is almost invariable in dynamic loading, the cracking is governed by a maximum tensile strain criterion. Then, the response of concrete under tensile stresses is assumed to be linear elastic until the fracture surface is reached (see Fig. 2(a)) and then, its behavior is characterized by an orthotropic material. Cracks are assumed to occur in planes perpendicular to the direction of the maximum tensile strain as soon as this strain reaches the specified concrete tensile strain ε_{ct}. After cracking has occurred the elastic modulus and Poisson's ratio are assumed to be zero in the perpendicular direction to the cracked plane, and a reduced shear modulus is employed. Due to bond effects, cracked concrete carries, between cracks, a certain amount of tensile force normal to the cracked plane. This effect is considered through a relationship between the strain and the stress normal to the cracking plane direction via a softening rule, as shown in Fig. 3(a). In this figure, f_t is the maximum tensile stress associated to the tensile strain ε_{ct} and the normal stress σ_j is determined from the current strain ε_j as established in the following expression

$$\sigma = f_t e^{\frac{-(\varepsilon_j - \varepsilon_{ct})}{\alpha}} \tag{14}$$

where α is a softening parameter obtained from the concept of concrete fracture energy G_f, property which is determined based on the characteristic length of the representative point under consideration. The use of the fracture energy guarantees that the numerical response will be independent of the finite element mesh (Cervera 1986, Tamayo *et al*. 2013a, b). Under transient loading, the interaction of the cracked sampling points and the redistributions of stresses due to cracking at previously uncracked points may cause closing of the existing cracks or re-opening of previously closed cracks for further loading. During the softening stage a record of the maximum tensile stress and strain is kept. If the current strain is smaller than its reference value, then the new stress is following the secant unloading path (see Fig. 3(a)). An open crack is allowed to close if the value of the normal strain across the crack is compressive. For any strain smaller than ε_j stress is interpolated according to the secant path. Upon further loading, if the value of the current strain exceeds the value ε_j the stress is calculated as before according to Eq. (14) and the reference values

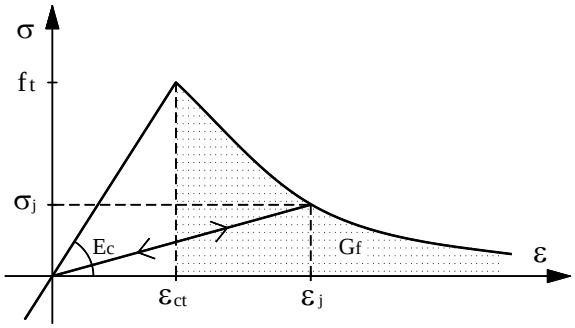

(a) Tension stiffening model for concrete via a softening rule

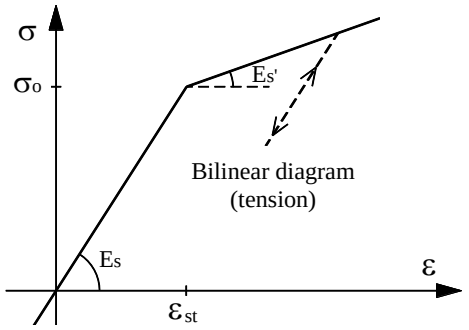

(b) Constitutive law for steel reinforcement

Fig. 3 Constitutive laws for concrete and steel materials

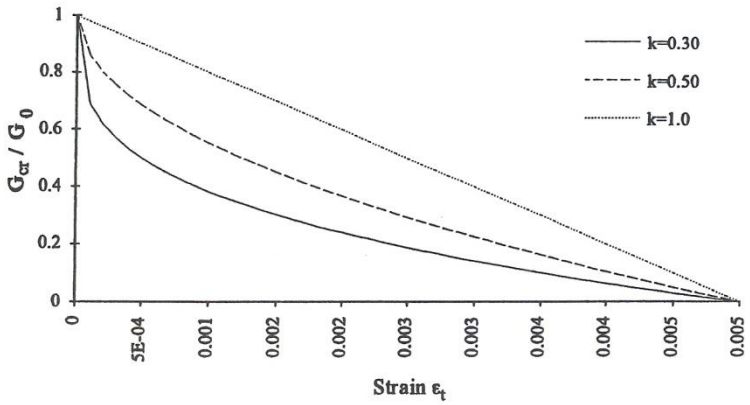

Fig. 4 Shear transfer model: Shear modulus versus crack normal tensile strain for various values of exponent *k* (shear retention model adapted from Tamayo 2015)

of stress and strain are updated. The steel reinforcement is modeled as a one-dimensional elasto-plastic material with a constant elastic modulus E_s and a tangential modulus $E_{s'}$ according to the bilinear stress-strain relation shown in Fig. 3(b). This relation is the same for tension and compression stresses and hysteretic loops are allowed to be formed.

During fracture propagation in reinforced concrete, shear tractions can arise across the cracking surfaces taking place aggregate interlock and dowel action. A simple implementation of these phenomena into the smeared crack approach is to assume a constant value of the shear modulus after cracking. Some authors consider that in the full shear retention model, the shear modulus is constant and its value is equal to that of the uncracked shear modulus G_o, while in the no shear retention model, the shear modulus is null after cracking. Both models may be criticized for their unreliability, since in these cases the shear modulus at cracking is given by an arbitrary estimation. To overcome this difficulty a modified model is adopted considering a decreasing power function for the shear stiffness across the cracked plane as a function of the normal cracking strain ε_t (see Fig. 4). Obviously, for an increased value of ε_t the ability of concrete to transfer shear stresses is reduced. According to this power law the reduced shear modulus G_{cr} can be expressed as a function of the initial shear modulus G_o by the following expression

$$G_{cr} = \left\{1 - \left(\varepsilon_t / \varepsilon_{su}\right)^k\right\} G_o \tag{15}$$

where ε_t is the normal tensile strain at the cracking zone, k is a parameter that varies between 0.30 and 1.0 and the value ε_{su} can be taken equal to 0.005. In this investigation, a no shear retention model is used if any other specification is given.

2.1 Numerical simulation procedure

In order to introduce the implicit numerical algorithm for the solution of the nonlinear dynamic equation, it is necessary to describe the predictor and corrector form of the Newmark scheme for the integration of the semi-discrete system of governing equations. Typically, at time station t_{n+1} these equations take the following form (Tamayo 2015)

$$\boldsymbol{M}\boldsymbol{a}_{n+1} + \boldsymbol{C}\boldsymbol{v}_{n+1} + \int \boldsymbol{B}^T \boldsymbol{\sigma}_{n+1}(\boldsymbol{d}_{n+1}) d\Omega = \boldsymbol{f}_{n+1} \tag{16}$$

where $\boldsymbol{M}$ and $\boldsymbol{C}$ are the mass and damping matrices, respectively while $\boldsymbol{a}_{n+1}$, $\boldsymbol{v}_{n+1}$ and $\boldsymbol{d}_{n+1}$ are the acceleration, velocity and displacement vectors, respectively, and the vectors $\boldsymbol{\sigma}_{n+1}$ and $\boldsymbol{f}_{n+1}$ represent the stresses and the external forces. The tangential stiffness matrix $\boldsymbol{K}_{et}$ is related to the internal forces in the following manner

$$\boldsymbol{K}_{et} \Delta \boldsymbol{d}_n = \int \boldsymbol{B}^T \boldsymbol{\sigma}_{n+1}(\boldsymbol{d}_{n+1}) d\Omega - \int \boldsymbol{B}^T \boldsymbol{\sigma}_n(\boldsymbol{d}_n) d\Omega \tag{17}$$

with,

$$\boldsymbol{K}_{et} = \int \boldsymbol{B}^T \boldsymbol{D}_{et} \boldsymbol{B} d\Omega \tag{18}$$

In the Newmark scheme displacement and velocity at time t_{n+1} can be expressed in the following form

$$\boldsymbol{d}_{n+1} = \tilde{\boldsymbol{d}}_{n+1} + \Delta t^2 \beta \boldsymbol{a}_{n+1} \tag{19}$$

$$\boldsymbol{v}_{n+1} = \tilde{\boldsymbol{v}}_{n+1} + \Delta t \gamma \boldsymbol{a}_{n+1} \tag{20}$$

with

$$\tilde{\boldsymbol{d}}_{n+1} = \boldsymbol{d}_n + \Delta t \boldsymbol{v}_n + \Delta t^2 (1/2 - \beta) \boldsymbol{a}_{n+1} \tag{21}$$

$$\tilde{\boldsymbol{v}}_{n+1} = \boldsymbol{v}_n + \Delta t (1 - \gamma) \boldsymbol{a}_n \tag{22}$$

Note that $\boldsymbol{d}_n$, $\boldsymbol{d}_{n+1}$ and $\boldsymbol{d}_{n+1}$ are the approximations to $\boldsymbol{d}(t_n)$, $\dot{\boldsymbol{d}}(t_n)$ and $\ddot{\boldsymbol{d}}(t_n)$ and β and γ are free parameters which control the accuracy and stability of the method. $\tilde{\boldsymbol{d}}_{n+1}$ and $\tilde{\boldsymbol{v}}_{n+1}$ are the predictor values and $\boldsymbol{d}_{n+1}$ and $\boldsymbol{v}_{n+1}$ are the corrector values. Initially, displacements $\boldsymbol{d}_0$ and velocities $\boldsymbol{v}_0$ are provided and the acceleration $\boldsymbol{a}_0$ is obtained from the following expression

$$\boldsymbol{M}\boldsymbol{a}_0 = \boldsymbol{f}_0 - \boldsymbol{C}\boldsymbol{v}_0 - \boldsymbol{K}_e \boldsymbol{d}_0 \tag{23}$$

where $\boldsymbol{K}_e$ is the elastic stiffness matrix of the system. By using Eqs. (16)-(22), an effective static problem is formed which is solved using a Newton Raphson scheme. This algorithm may be summarized in the following manner:

1. Set iteration counter i=0
2. Begin predictor phase in which we set

$$\boldsymbol{d}_{n+1}^{i} = \tilde{\boldsymbol{d}}_{n+1} = \boldsymbol{d}_{n} \tag{24}$$

$$\boldsymbol{v}_{n+1}^{i} = \tilde{\boldsymbol{v}}_{n+1} = \boldsymbol{v}_{n} \tag{25}$$

$$\boldsymbol{a}_{n+1}^{i} = \left(\boldsymbol{d}_{n+1}^{i} - \tilde{\boldsymbol{d}}_{n+1}\right)/(\Delta t^{2}\beta) \tag{26}$$

3. Evaluate residual forces

$$\boldsymbol{\psi}^{i} = \boldsymbol{f}_{n+1} - \boldsymbol{M}\boldsymbol{a}_{n+1}^{i} - \boldsymbol{C}\boldsymbol{v}_{n+1}^{i} - \int \boldsymbol{B}^{T}\boldsymbol{\sigma}_{n+1}^{i}\left(\boldsymbol{d}_{n+1}^{i}\right)d\Omega \tag{27}$$

4. If required, form the effective stiffness matrix using the following expression

$$\boldsymbol{K}^{*} = \boldsymbol{M}/(\Delta t^{2}\beta) + \gamma\boldsymbol{C}_{T}/(\Delta t\beta) + \boldsymbol{K}_{T}(\boldsymbol{d}_{n+1}^{i}) \tag{28}$$

5. Factorize, forward reduction and back substitute as required to solve

$$\boldsymbol{K}^{*}.\Delta\boldsymbol{d}^{i} = \boldsymbol{\psi}^{i} \tag{29}$$

6. Enter corrector phase in which we set

$$\boldsymbol{d}_{n+1}^{i+1} = \boldsymbol{d}_{n+1}^{i} + \Delta\boldsymbol{d}^{i} \tag{30}$$

$$\boldsymbol{a}_{n+1}^{i+1} = \left(\boldsymbol{d}_{n+1}^{i} - \tilde{\boldsymbol{d}}_{n+1}\right)/\left(\Delta t^{2}\beta\right) \tag{31}$$

$$\boldsymbol{v}_{n+1}^{i+1} = \boldsymbol{v}_{n} + \Delta t\gamma\boldsymbol{a}_{n+1}^{i+1} \tag{32}$$

7. If $\Delta\boldsymbol{d}^{i}$ and/or ψ^{i} do not satisfy the convergence conditions then set i=i+1 and go to step 3, Otherwise continue. Set

$$\boldsymbol{d}_{n+1} = \boldsymbol{d}_{n+1}^{i+1} \tag{33}$$

$$\boldsymbol{v}_{n+1} = \boldsymbol{v}_{n+1}^{i+1} \tag{34}$$

$$\boldsymbol{a}_{n+1} = \boldsymbol{a}_{n+1}^{i+1} \tag{35}$$

8. Set n=n+1, form $\boldsymbol{C}.\boldsymbol{v}_{n+1} + \int \boldsymbol{B}^{T}\boldsymbol{\sigma}_{n+1}(\boldsymbol{d}_{n+1})d\Omega$ and begin the next time step.

In this work, when the nuclear containment shell is subjected to the action of an earthquake load, the Johnson-Epstein sinesweep analytical earthquake will be used as a prescribed horizontal acceleration history at the base of the structure. The sinesweep accelerogram is energetically equivalent to the El Centro accelerogram with a maximum acceleration level of 0.33 g, as it is shown in Fig. 5, and whose values are defined as

$$\ddot{d}_{g}(t) = \ddot{d}_{\max}^{g}(\omega)\left[\sin(\theta(t))\right] \tag{36}$$

where

$$\omega = \dot{\theta}(t)/2\pi \tag{37}$$

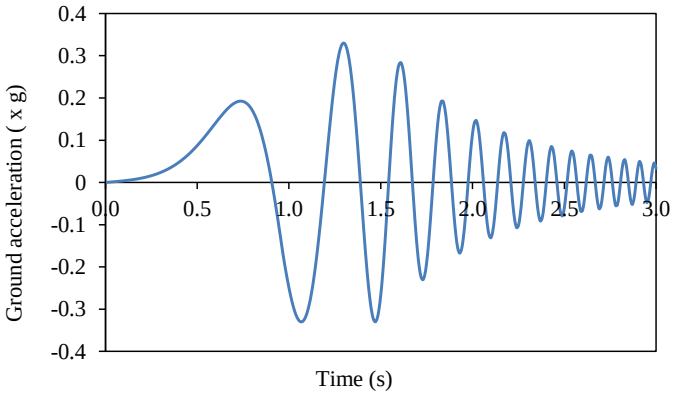

Fig. 5 Sine sweep earthquake

$$\theta(t) = At + Bt^N \tag{38}$$

$$\ddot{d}^g_{\max} = 0.22\omega.g \qquad \omega < 1.5 \tag{39}$$

$$\ddot{d}^g_{\max} = 0.33.g \qquad 1.5 < \omega < 3.5 \tag{40}$$

where, $\ddot{d}_g(t)$ is the ground acceleration time history, $\ddot{d}^g_{\max}$ is the maximum ground acceleration as a function of specific forcing frequency ω, g is the acceleration due to gravity and $\sin(\theta(t))$ is the variable frequency sinusoidal signal. The free parameters A and B in Eq. (38) are defined as 1.0 and 3.0, respectively, with N=3.0. In addition, the generalized force $\boldsymbol{f}_{n+1}$ due to earthquake load on the right hand side of Eq. (27) is defined in the following manner:

$$\boldsymbol{f}_{n+1} = -\boldsymbol{M}\boldsymbol{I}\ddot{d}_g(t) \tag{41}$$

where $\boldsymbol{M}$ is the mass matrix and $\boldsymbol{I}$ is a vector indicating the direction of the earthquake component.

4. Numerical examples

4.1 Reactor containment shell subjected to aircraft impact (Cervera et al. 1988)

The horizontal impact of an aircraft (Boeing 707-320, Cervera *et al*. 1988) on the shield building of a nuclear power plant is analyzed. The geometry, the loading function and the reinforcement are specified in Fig. 6. The built-in reinforced concrete shell is composite of cylindrical and spherical parts of constant thickness. The reinforcement placed circumferentially and meridionally on the interior and exterior surfaces consist of bars of 40 mm diameter, spaced at 8 cm. The material properties are shown in Table 1. The impact is assumed to occur horizontally and is analyzed following an uncoupled approach in which its effect onto the nuclear containment is considered through the application of an impact load function (see e.g., Cervera 1986, Abbas *et al*. 1996, Kukreja 2005). The location of the area of impact of 28 m^2 is also shown in Fig. 6. The load history is also indicated and it is noted that the load has a maximum value of 9000 ton. Since

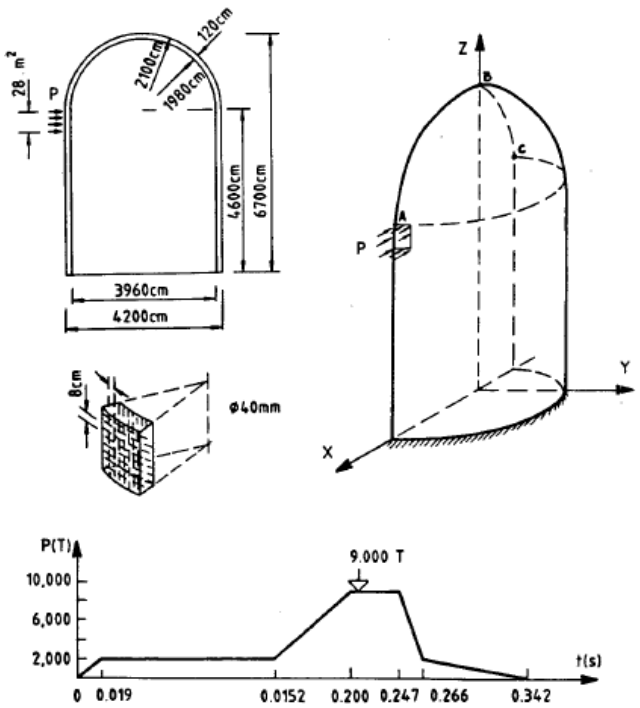

Fig. 6 Nuclear containment structure: general layout and loading time history for aircraft impact taken from Cervera (1986)

Table 1 Material properties (kN, m)

Concrete	Steel
Elastic modulus E_c=30×10^6	Elastic modulus E_s=21×10^7
Poisson's coefficient ν=0.17	Tangential modulus E_s=0.0
Ultimate compressive strength f_c=35000	Yield stress σ_o=460000
Ultimate tensile strain ε_{ct}=0.0002	
Ultimate compressive strain ε_u=0.0035	
Fracture energy G_f=0.20	

the loading and geometry of the shell are symmetric, only one half of the structure is modeled. Therefore, the applied distributed load is defined in a rectangular area of 14 m^2. The implicit Newmark scheme with β=0.5 and γ=0.5 is used to integrate the equilibrium equations in time with a time step of Δt=0.00475 s. The selected time step corresponds to T/50, where T is the fundamental period of the structure, which is equal to 0.23 s.

A proper mesh convergence study is carried out in order to verify the adequacy of the finite element mesh. For this purpose, three finite element meshes with 625 (mesh 1), 2500 (mesh 2) and 7500 (mesh 3) 20-node hexahedral finite elements are considered (see Fig. 7). The numbers of equations to solve in each case are 13250, 82900 and 158000, respectively. Firstly, an elastic analysis is carried out and the maximum computed horizontal displacements for the control point A are -3.138 cm, -3.140 cm and -3.135 cm for mesh 1, mesh 2 and mesh 3, respectively. When the

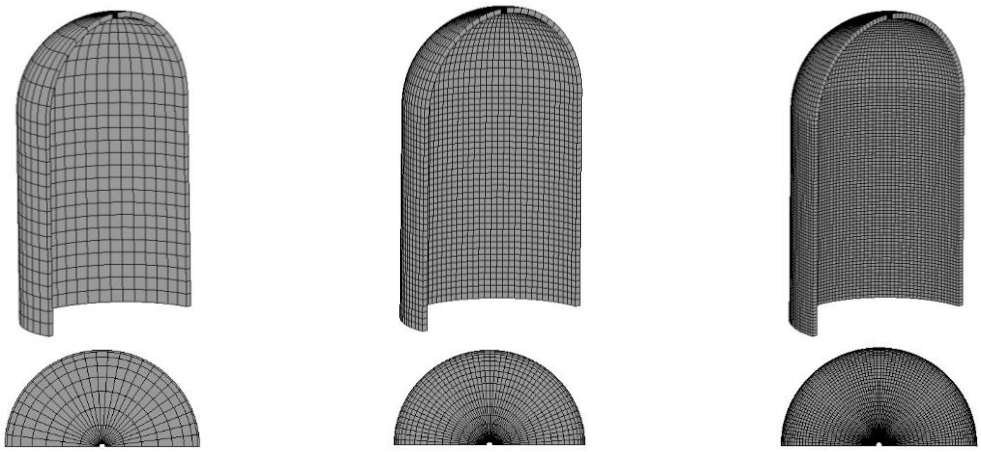

(a) Mesh 1 (625 elements) (b) Mesh 2 (2500 elements) (c) Mesh 3 (7500 elements)

Fig. 7 Three-dimensional and plant view of finite element meshes

nonlinear behavior of concrete is considered with a cracking strain of 0.0002, these displacements are -4.78 cm,-4.56 cm and -4.57 cm, respectively. Other results expressed in terms of cracking patterns and concrete stresses at the outer walls of the nuclear containment are found to be similar for the three meshes. Next, a similar analysis was carried out for the seismic load case (see next section) and similar results were also found for the three meshes. In this manner, the objectivity of the finite element results with the present numerical model is proved. Because all meshes yielded similar results, any mesh can be used in the analysis. However, mesh 3 is preferred to verify examples, while for parametric studies (where several runs are needed, as in section 4.3) mesh 1 can be used to save computational time. A typical simulation with mesh 3 for the seismic load case took about 3 CPU hours on a notebook Intel core i5 (Inspiron 14-3000) with 4 preprocessors.

As commented before, the problem was analyzed previously by other researchers. Precisely, in Table 2 is presented a summary of the main characteristics of the numerical and constitutive models used by other references and those presented in this work. Only studies where hexahedral finite elements were used are listed. It may be observed that various studies have used a reduced number of finite elements in the numerical modeling in conjunction with an elasto-viscoplastic algorithm for the stress integration of steel and concrete. Nevertheless, Rebora and Zimmerman (1976) employed an elasto-plastic algorithm besides a cracking monitoring algorithm based on a maximum stress criterion where strain rate effects were omitted. Other authors have used hipoelasticity (Kukreja 2005) and damage plasticity (Iqbal *et al*. 2012) for modeling concrete. All works listed in Table 2 employed a particular computer code with exception of the work of Iqbal *et al*. (2012), where the commercial software ABAQUS was used. In the present work, elasto-plasticity is adopted for modeling reinforced concrete. Concrete cracking is based on a maximum strain criterion and strain rate effects were included in the material model by using the numerical algorithm proposed by Liu (1985). To sum up, the present constitutive model combines different features from other constitutive models found in the technical literature (see e.g. Tamayo 2013a, b and Dias *et al*. 2015). Although the finite element mesh is not extremely refined in the present study, it is significantly comprised of more elements than previous works.

Horizontal displacements at monitoring points A, B and C (these points are defined in the

Table 2 Details of the discretization and numerical modeling

Items	Rebora and Zimmerman (1976)	Cervera *et al.* (1988)	Abbas *et al.* (1996)	Pandey *et al.* (2006)	Kukreja (2005)	Iqbal *et al.* (2012)	Present analysis
Finite element discretization							
Nodes per element	20	20	20	20	20	20	20
Number of elements	38	52	52	54	400	514640	7500
Tensile cracking modeling							
Smeared	yes	yes	yes	yes	yes	yes	yes
Cracking Criterion	stress	strain	strain	strain	--	stress	strain
TSOF/ TSTIF(1)	TSOF	TSOF	TSOF	TSOF+ TSTIF	TSOF	--	TSOF+ TSTIF
Model: Elasto-plastic(EP)/Elasto-viscoplastic (EVP)/Hipoelastic (HE)/Damage-plasticity (DP)							
Concrete	EP	EVP	EVP	EVP	HE	DP	EP
Failure criterion(2)	S	D-P	WW	MW	uniaxial	uniaxial Sinha	D-P
Deviatoric Section	noncircular	circular	noncircular	noncircular	--	--	circular
Strain rate effect?	No	yes	Yes	Yes	--	Yes	yes
Steel	EP	EVP	EVP	EVP	EP	EVP	EP
Solution procedure: Newmark (N) – Explicit (E) – Wilson Θ (W)							
Time integration	W	N	N	--	--	--	N
G.I.(3)	27	15	15	--	--	1	8
EL/IL(4)	IL	EL/IL	IL	IL	IL	IL	EL/IL

(1) TSOF/TSTIF: Tension softening / tension stiffening
(2) D-P/WW/MW/S: Drucker-Prager / Willam and Warnke / Menetrey and Willam / Saugy
(3) G.I: Gaussian integration
(4) EL/IL: earthquake load / impact load

spherical part as shown in Fig. 6) as functions of time obtained with the present numerical model and those obtained by Kukreja (2005) are compared and plotted in Fig. 8. In Kukreja (2005), a different material model and a finite element mesh composed of 400 20-node hexahedral finite elements were used. All these results correspond to a maximum tensile concrete strain of 0.0002 and to a fracture energy of 0.2 kN/m. Moreover, in Abbas *et al*. (1996) history of normal stress components σ_x, σ_y and σ_z at different surfaces of the containment near the vicinity of the impact zone are presented. Precisely, in Figs. 9-11 are compared these stresses with those obtained in the present work for external, middle and internal surfaces, respectively. The spatial distributions for stress components σ_z and σ_y for an analysis time of 0.25s (time in which the maximum lateral displacement in the impact zone occurred) are shown in Figs. 12(a)-(b), respectively. Deformed shapes of the containment for times 0.25 s and 0.56 s (end of the analysis) are presented in Figs. 13-14, respectively.

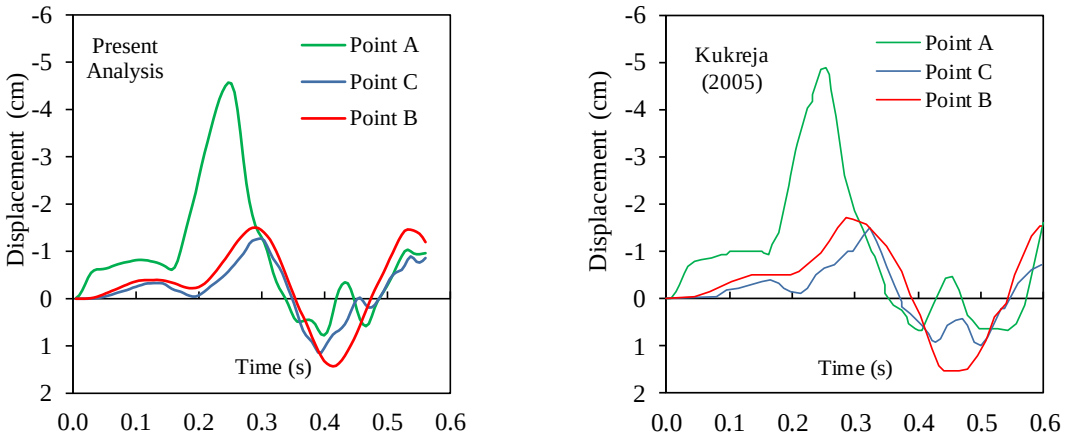

(a) Present analysis (b) Kukreja (2005)

Fig. 8 Nonlinear analysis: lateral displacements at points A, B and C

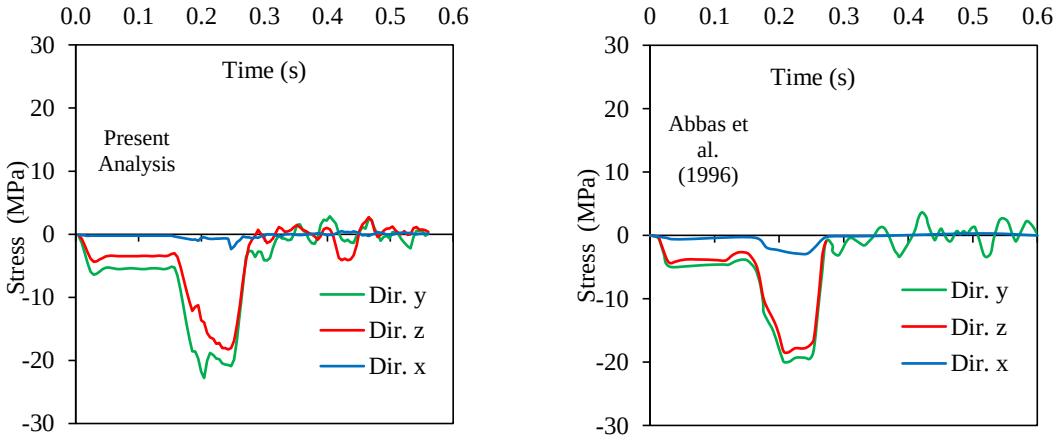

Fig. 9 History of stresses at external surface

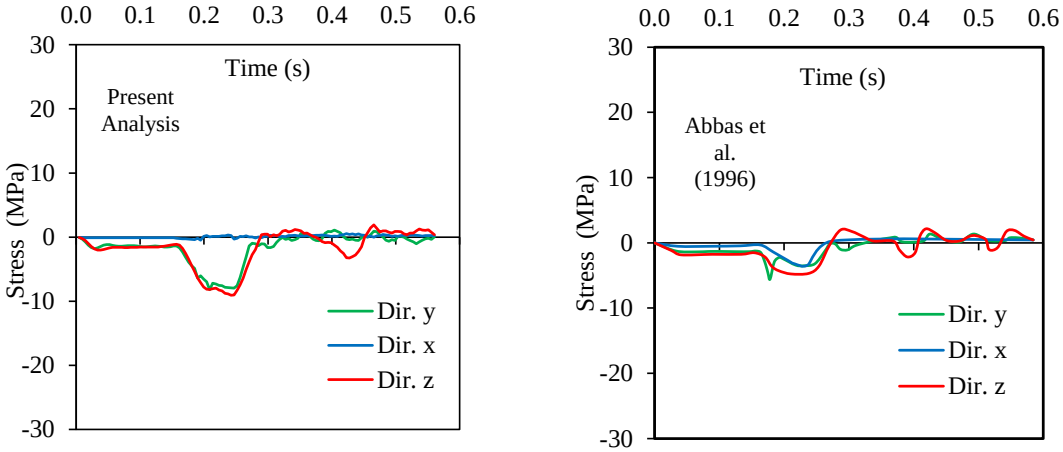

Fig. 10 History of stresses at middle surface

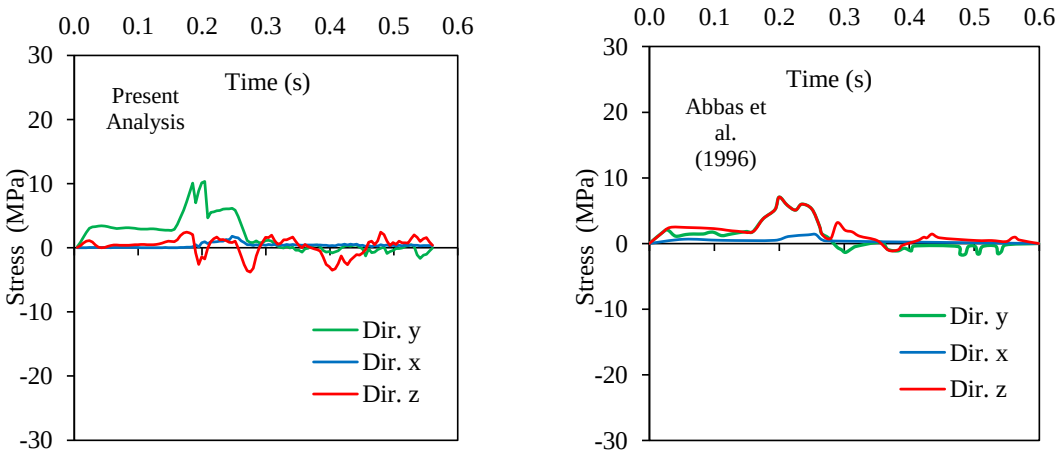

Fig. 11 History of stresses at internal surface

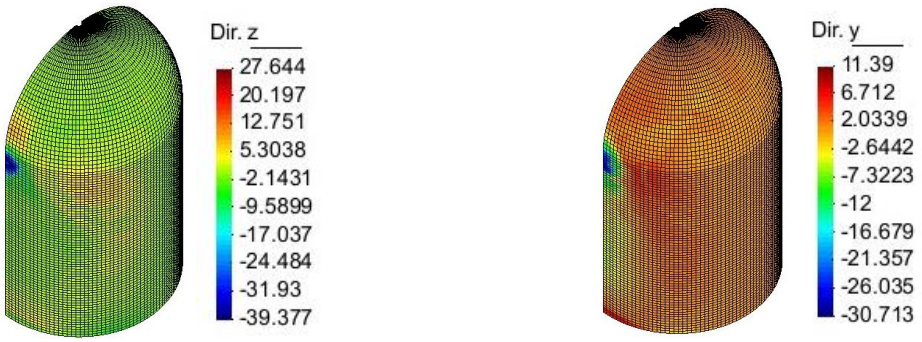

(a) Stress σ_z (MPa) (b) Stress σ_y (MPa)

Fig. 12 Stress distribution for maximum lateral displacement at 0.25 s

(a) Isometric view (b) Back view

Fig. 13 Lateral displacements (cm) at 0.25 s. (magnification factor: 120)

Fig. 15 depicts the cracking patters obtained with the present numerical model and those published by Cervera *et al*. (1988) for times of 0.56 s and 0.38 s, respectively. It is important to mention that in Cervera *et al*. (1988) two maximum cracking strains were used (0.0002 and

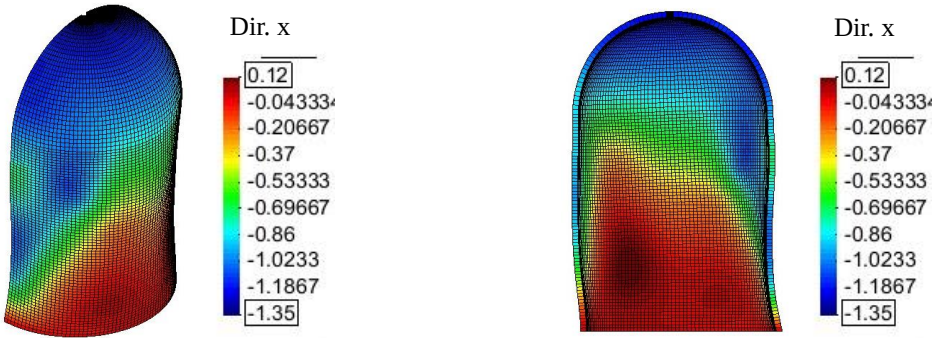

(a) Isometric view (b) Back view

Fig. 14 Lateral displacements (cm) at 0.56 s. (magnification factor: 200)

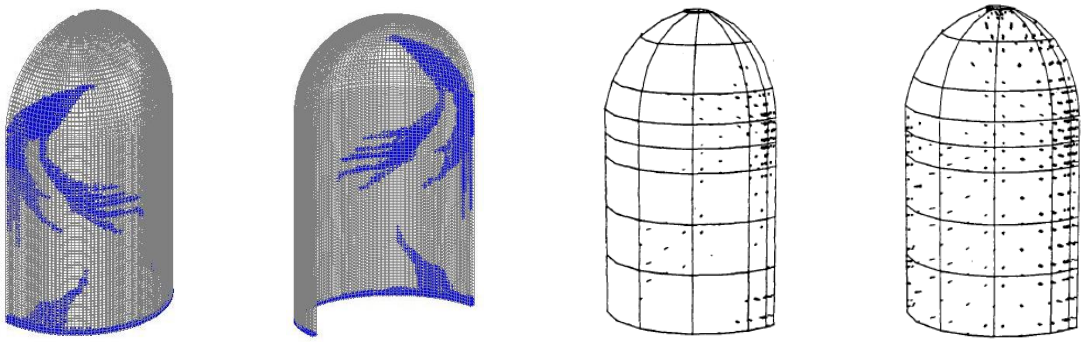

(a) External face (present analysis at 0.56 s for a maximum tensile strain of 0.0002)

(b) Internal face (present analysis at 0.56 s for a maximun tensile strain of 0.0002)

(c) External face (Cervera 1986 at 0.38 s for a maximum tensile strain of 0.0002)

(d) External face (Cervera 1986 at 0.38 s for a maximun tensile strain of 0.00015)

Fig. 15 Cracking patterns for concrete containment

0.00015). It may be observed that there are some differences in the cracking configuration for both responses and these may be attributed to the different number of finite elements used, the kind of integration rule and the chosen maximum tensile strain. Nevertheless, all results show that concrete cracking spreads out from the impact zone towards the base of the containment and to the upper region of the spherical part. The numerical results obtained in the present example in terms of lateral displacements, stresses and cracking patterns are in close agreement with results presented in other references.

4.2 Reactor containment shell under earthquake loading (Liu 1985)

The same containment shell previously analyzed for impact load is now analyzed for earthquake load with the load function shown in Fig. 5. This load function is applied at the base of the structure as a prescribed acceleration. For this purpose, it is supposed that the nuclear containment is supported by a rigid soil. The same geometry and mesh reinforcement of the previous example is also used. The selected time step for the analysis is 0.01 s which correspond

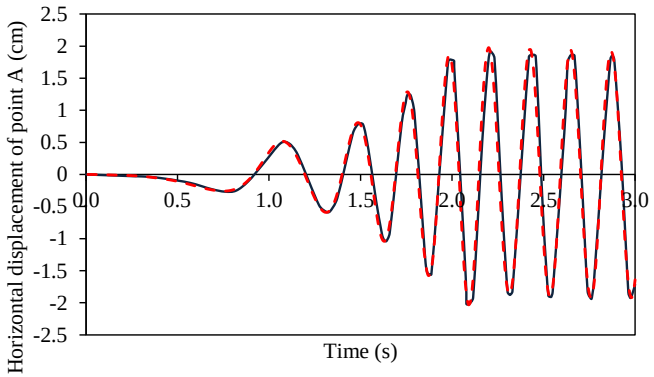

(a) Linear response

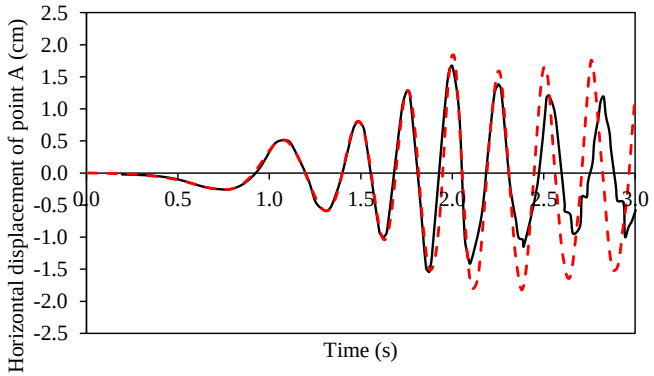

(b) Nonlinear response

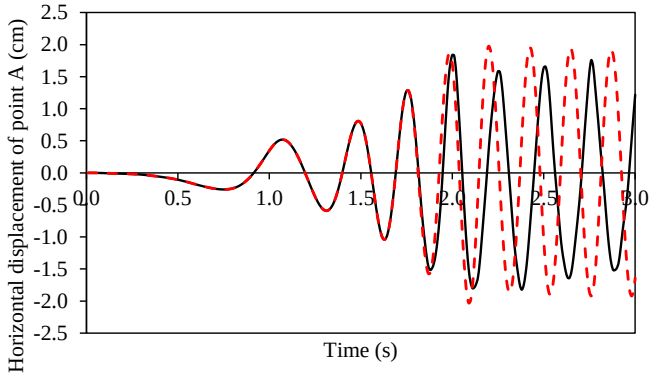

(c) Comparison for linear and nonlinear responses

Fig. 16 Nuclear containment structure under seismic load: Horizontal displacement at point A

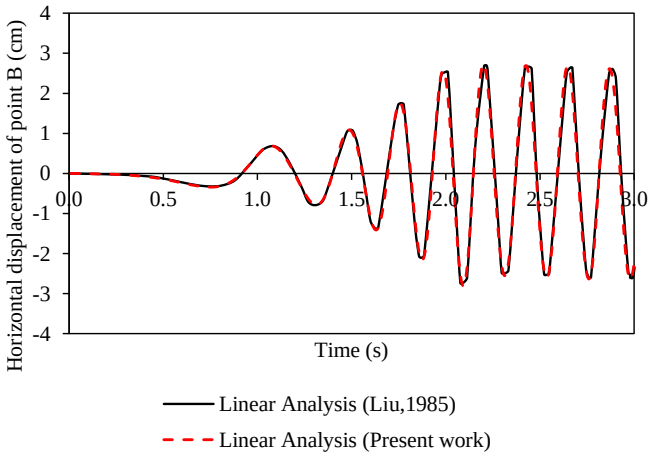

(a) Linear response

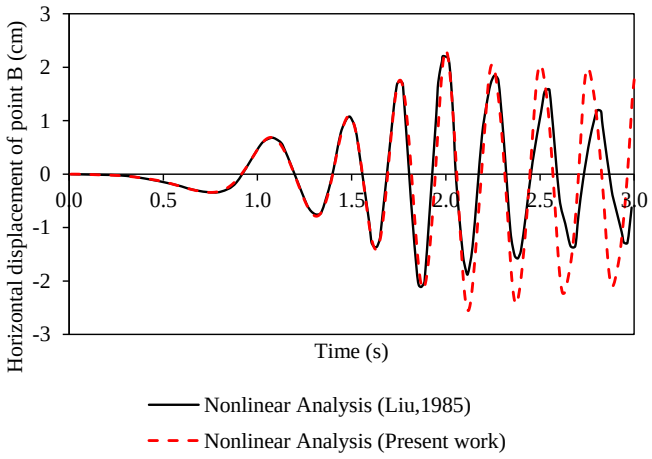

(b) Nonlinear response

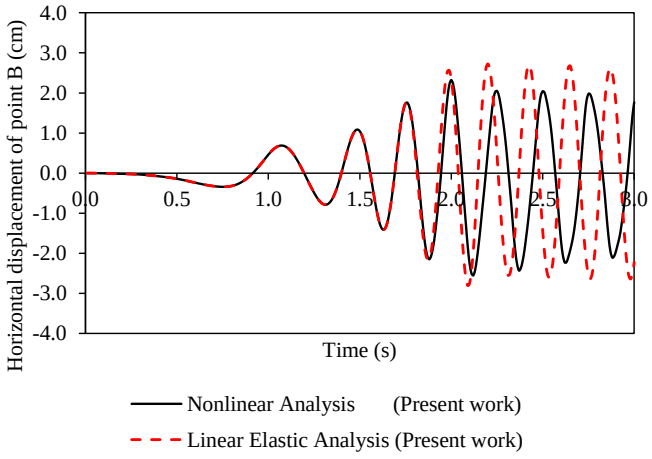

(c) Comparison for linear and nonlinear responses

Fig. 17 Nuclear containment structure under seismic load: Horizontal displacement at point B

to the value of $T/23$, where T is the fundamental period of the structure (Cervera *et al*. 1988). The implicit Newmark algorithm with β=0.25 and γ=0.50 is used. The nonlinear analysis was performed considering an ultimate tensile concrete strain of 0.00018. In Figs. 16(a)-(b) is compared the horizontal displacement history of point A obtained in the present work with that reported by Liu (1985) for the linear and nonlinear cases, respectively. In Fig. 16(c), present results for the linear and nonlinear cases are superimposed. As it can be seen, the vibration period is elongated and some dissipation due to nonlinear effect is evident. Also, the amplitude is smaller in the nonlinear analysis with respect to the linear case. Cracking affects the stiffness of the structure, changing its fundamental period. It is important to mention that in Liu (1985), shell finite elements were used in the numerical modeling. Similar results are depicted in Fig. 17, but now for the control point B. Comparisons of the linear and nonlinear responses obtained with the present model compare well with those obtained by Liu (1985) in terms of horizontal displacements.

Finally, Fig. 18(a) shows the evolution of cracking patterns along time obtained with the present numerical model. In Fig. 18(b), the crack patterns obtained in Cervera *et al*. (1988), where only 40 20-node solid finite elements were used, are also shown. As it can be seen, both numerical models predict the progressively development of cracking from the left to the right side at the base of the containment.

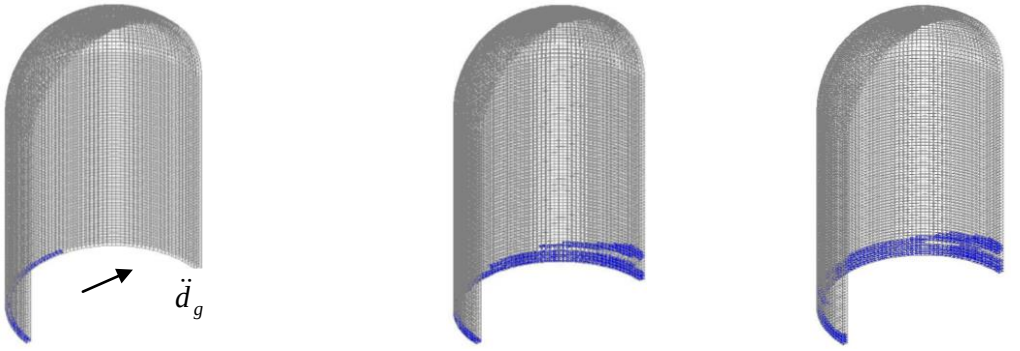

t=1.80 s *t*=1.95 s *t*=3.0 s

(a) Present analysis

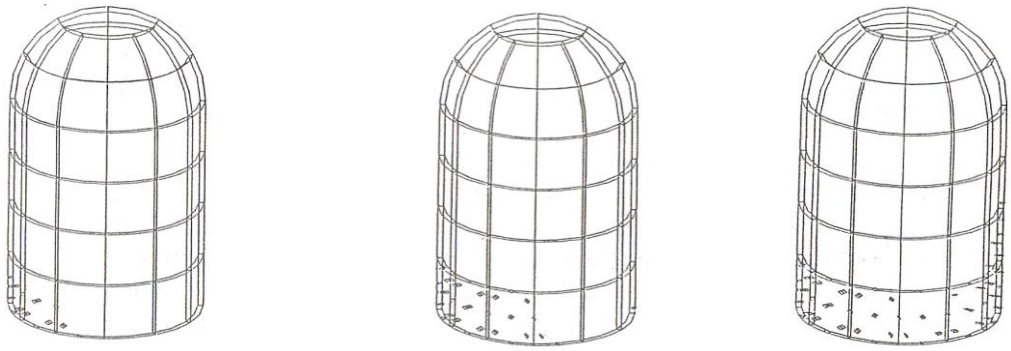

t=1.65 s *t*=1.80 s *t*=1.95 s

(b) Cervera *et al*. (1988)

Fig. 18 Crack patterns at different times for concrete with a cracking strain of 0.00018

4.3 Parametric study

4.3.1 Influence of shear retention

It may be interesting to investigate how the shear retention model used for cracked concrete affects the global responses of the Mark III containment. For the impact load case, the impact force is acting along the *x*-direction and the deformation of the structure follows this direction near the impact zone. According to the work of Iqbal *et al*. (2012), normal stress components in the *y* and *z* directions are found to be dominant near the impact zone while other stresses are almost negligible. Shear stresses become dominant as the distance from the impact location increases. According to Abbas *et al*. (1996), the shear stress component τ_{yz} is negligible and the other two shear stresses, which correspond to the punching stresses, are obviously localized in the impact area with a maximum value of 5 MPa. All these previous findings are consistent with the present numerical results.

Figs. 19-20 show the history of horizontal displacements of points A and B and the history of shear stress components τ_{yz} and τ_{xz}, respectively. These results are obtained by using the full shear retention, no shear retention and partial retention models. For full shear retention, the shear modulus of cracked concrete is assumed to be the same as that of intact concrete after concrete cracking. For no shear retention, the shear modulus of cracked concrete is assumed to be zero although a minimum value is used (10% of the shear modulus of intact concrete according to Cervera *et al*. 1988). The partial retention model follows the descending curve shown in Fig. 4 taking *k* equal to 0.3. As it may be observed, all models almost predict the same responses. For the seismic load case, the same analysis was carried out and Fig. 21 shows the history of horizontal displacements of points A and B. Again, similar results are obtained.

4.3.2 Influence of a base slab

In previous sections, the containment is modeled including only the dome and the cylinder. Hence, it may be interesting to perform the finite element analysis again considering a base slab and to assume that the bottom of the base slab is clamped to the ground directly. Alternatively, the

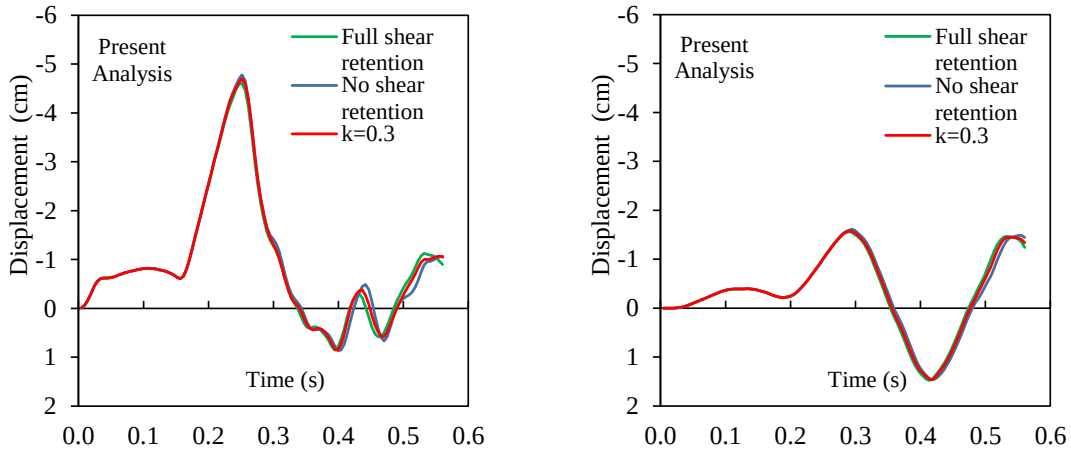

(a) Point A (b) Point B

Fig. 19 History of horizontal displacement at monitoring points (nonlinear analysis)

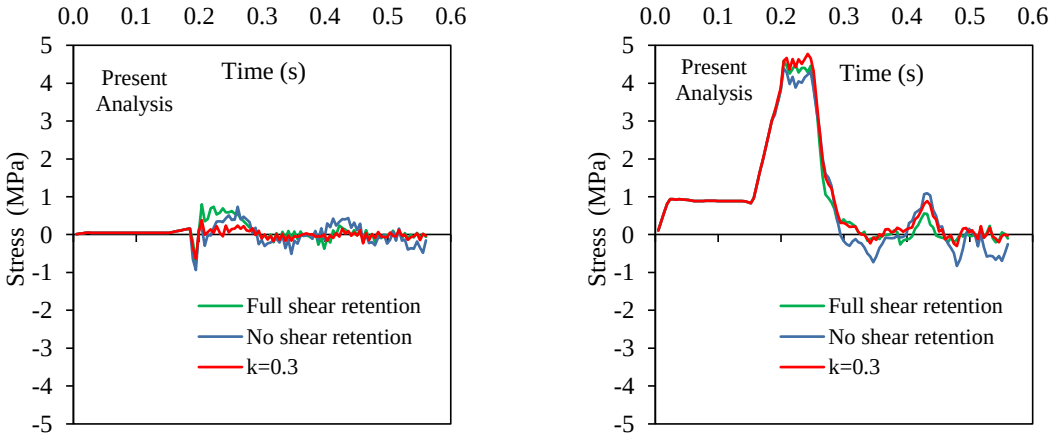

(a) Shear stress component τ_{yz} (b) Shear stress component τ_{xz}

Fig. 20 History of shear stresses τ_{yz} and τ_{xz} at external surface near the impact zone (nonlinear analysis)

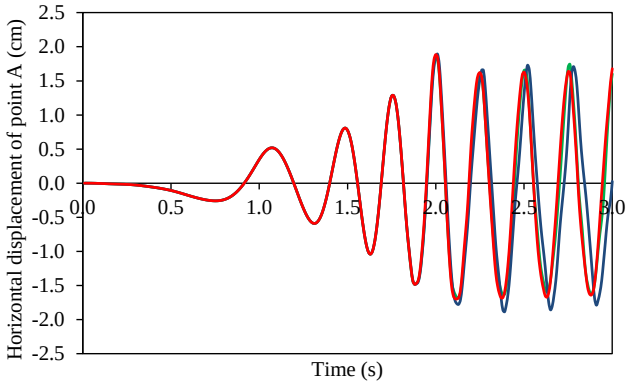

(a) Point A

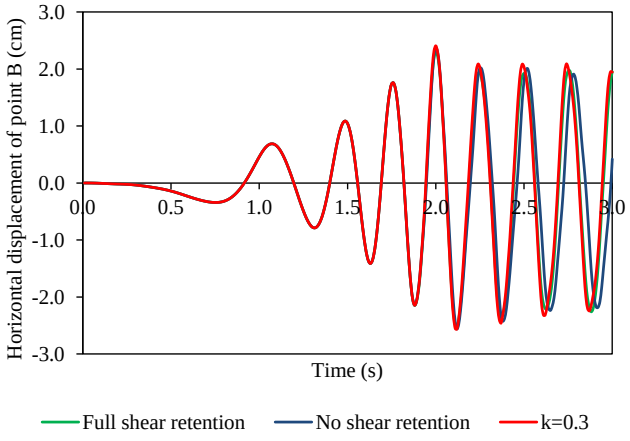

(b) Point B

Fig. 21 Nonlinear analysis of nuclear containment under seismic load: horizontal displacements

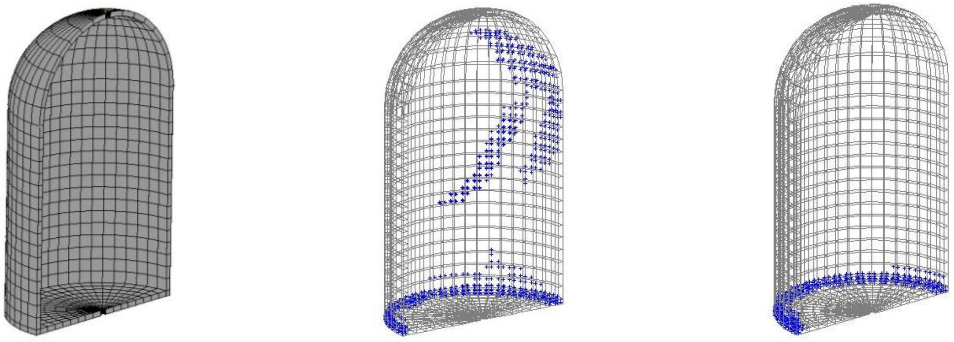

(a) Finite element mesh (b) impact load (c) seismic load

Fig. 22 Nuclear contaiment mesh and final cracking patterns for model with a RC base slab

bottom of the base slab can be also connected to the ground surface by using especial purpose 16-node zero thickness interface elements (Tamayo 2015). The interface elements allow the contact surfaces between the base slab and the ground to remain closed or open but no to penetrate each other. It was considered that the thickness of the base slab and its reinforcement mesh are similar to that of the concrete walls of the containment.

Fig. 22(a) shows the finite element mesh used in the analysis while Figs. 22(b)-(c) show the final cracking patterns obtained with present numerical model for the same impact and seismic actions of the previous sections, respectively. As it is observed, the obtained cracking patterns are very similar (especially for the impact load) to those obtained in previous sections without the consideration of the base slab. Nevertheless, it is clear that some cracking take place at the perimeter of the base slab near the junction of the slab with the cylinder wall.

For the impact load case, Fig. 23 shows the history of horizontal displacements of points A and B for three cases: 1) without the base slab; 2) with the base slab clamped to the ground directly and 3) with the base slab link to the ground by using contact elements where separation is allowed

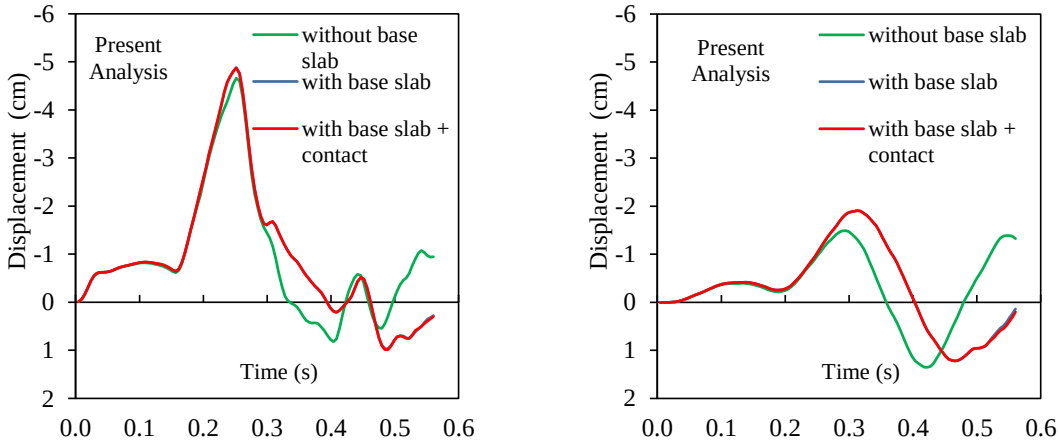

(a) Point A (b) Point B

Fig. 23 History of horizontal displacements at monitoring points (nonlinear analysis)

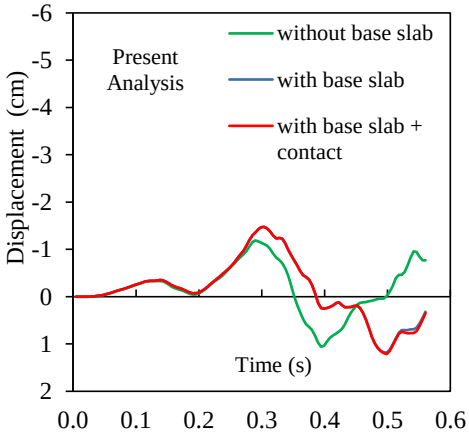

(a) Horizontal displacement at point C

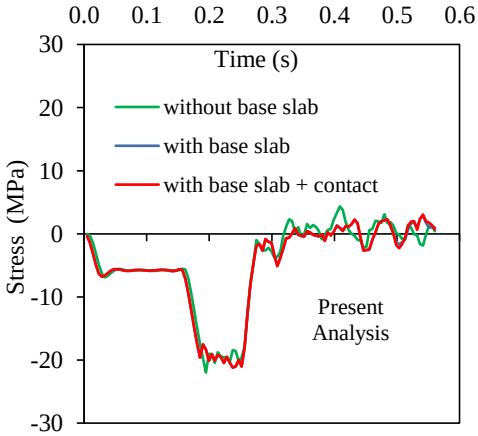

(b) Stress component σ_y at external surface

Fig. 24 Different results for nonlinear analysis of containment under impact load

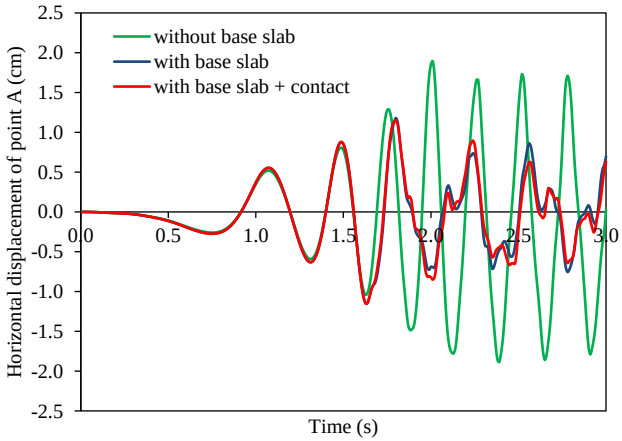

(a) Point A

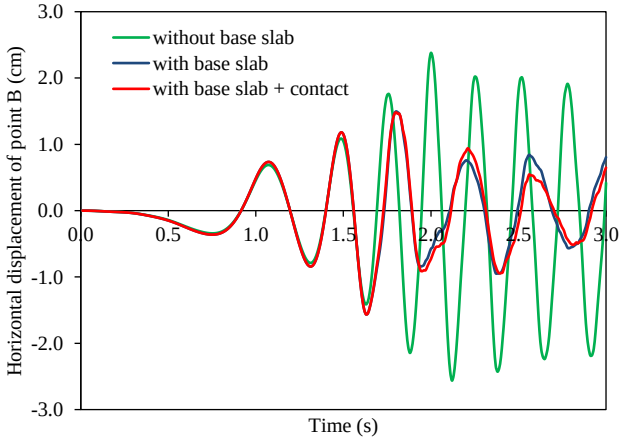

(b) Point B

Fig. 25 Nonlinear analysis of nuclear containment under seismic load: horizontal displacements

to occur. Figs. 24(a)-(b) show the history of horizontal displacement of point C and the history of stress component σ_y near the impact zone, respectively. A similar analysis was carried out for the seismic load case and corresponding results for points A and B are shown in Fig. 25. As can be seen, the consideration of the base slab with contact elements does not differ significantly from the case of the clamped base slab to the ground directly. Therefore, contact elements can be omitted with safety for the present examples. Moreover, for the impact load case, the inclusion of the base slab in the numerical model significantly modifies the horizontal displacements of monitoring points A, B and C after 0.3 s. However, the normal stress component σ_y in the vicinity of the impact zone remains almost unchanged independently of the base slab. For the seismic action, horizontal displacements at monitoring points A and B are significantly damped out after 1.75 s.

5. Conclusions

A three-dimensional numerical model for the nonlinear dynamic analysis of reinforced concrete containment shells under extreme loads is implemented and presented in this work. A 20-node brick finite element is used to model reinforced concrete containments. The material model considers strain rate effects and is based on the theory of plasticity, while a cracking monitoring algorithm based on the smeared cracking approach is used for tensile stresses. Nonlinear finite element analyses of the General Electric Mark III reinforced concrete containment are performed. Firstly, verification of the numerical model is done by analyzing this structure under impact and seismic actions and obtained results are compared with those published by other authors. Good agreement is found for both loading cases in terms of cracking patterns, history of stresses and lateral displacements. A parametric study is carried out in order to investigate the importance of the shear transfer model used for cracked concrete and the effect of a base slab incorporation in the numerical model. These aspects have not been previously investigated by other researches for the Mark III containment under impact and seismic actions. The main conclusions of this study are:

- A converge study was carried out and mesh independency of the finite element results was proved for the present material model.
- Because 20-node finite elements are computational expensive, the PARDISO software package was successfully implemented and incorporated into the present finite element code and full advantage of the number of preprocessor was taken.
- It was verified from the time history curves for the monitoring points in the earthquake loading case that the vibration period is elongated and some dissipation due to nonlinear effects occurs. Also, the amplitude is smaller in the nonlinear analysis than in the linear case. Cracking affects the stiffness of the structure, changing its fundamental period. The response to a seismic excitation is greatly dependent on the dynamic characteristics of the structure, as the energy absorbed by the system depends both on the forcing and the natural frequencies.
- Shear retention has very little influence on the horizontal displacements history at monitoring points for both loading cases. Also, localized shear stresses near the impact zone for the impact load case do not change significantly for any of shear retention models.
- For the calculation of stresses near the impact zone for the impact load case, the base slab may be excluded from the analysis of the containment and the cylinder part can be assumed to be clamped to the ground directly. Nevertheless, the base slab should be included in the analysis when a precise determination of horizontal displacements is needed. For the seismic load case, the horizontal displacements at the monitoring points are significantly damped out

after 1.75 s due to the base slab incorporation. Thus, the base slab should be considered in this case.

• For the sake of saving computer time, contact elements at the bottom of the base slab to permit separation at this contact surface may be excluded from the analysis and the base slab can be assumed to be clamped to the ground directly. This observation is supported by the fact that the inclusion of contact elements does not change considerably the global response of the containment for both loading cases. Nevertheless, their inclusion significantly increases the number of iterations of the nonlinear algorithm.

Acknowledgments

The financial support provided by CAPES and CNPq is gratefully acknowledged.

References

Abbas, H., Paul, D.K., Godbole, P.N. and Nayak, G.C. (1996), "Aircraft crash upon outer containment of nuclear power plant", *Nucl. Eng. Des.*, **160**(1), 13-50.

Cervera, M. (1986), "Nonlinear analysis of reinforced concrete structures using three dimensional and shell finite element models", Ph.D. Dissertation, Swansea University, Swansea.

Cervera, M., Hinton, E. and Bicanic, N. (1988), "Non-linear transient dynamic analysis of three dimensional structures", *Numerical Methods and Software for Dynamic Analysis of Plates and Shells*, E. Hinton, R.W., Pineridge Press, Swansea, U.K.

Dias, M.M., Tamayo, J.L.P., Morsch, I.B. and Awruch, A.M. (2015), "Time dependent finite element analysis of steel-concrete composite beams considering partial interaction", *Comput. Concrete*, **15**(4), 687-707.

Hu, H.T. and Liang, J.I. (2000), "Ultimate analysis of BWR Mark III reinforced concrete containment subjected to internal pressure", *Nucl. Eng. Des.*, **195**, 1-11.

Iqbal, M.A., Rai, S., Sadique M.R., and Bhargava, P. (2012), "Numerical simulation of aircraft crash on nuclear containment structure", *Nucl. Eng. Des.*, **243**, 321-335.

Kamagata, S. and Takewaki, I. (2013), "Ocurrence mechanism of recent large earthquake ground motions at nuclear power plant sites in Japan under soil-structure interaction", *Earthq. Struct.*, **5**(4), 557-585.

Kukreja, M. (2005), "Damage evaluation of 500 MWe Indian pressurized heavy water reactor nuclear containment for aircraft impact", *Nucl. Eng. Des.*, **235**(17-19), 1807-1817.

Liu, G.Q. (1985), "Nonlinear and transient finite element analysis of general reinforced concrete plates and shells", Ph.D. Dissertation, Swansea University, Swansea.

Manjuprasad, M., Gopalakrishnan, S. and Appa Rao, T.V.S.R (2001), "Nonlinear dynamic response of a reinforced concrete secondary containment shell subjected to seismic load", *Eng. Struct.*, **23**(5), 397-406.

Pandey, A.K. (2010), "Damage prediction of RC containment shell under impact and blast loading", *Struct. Eng. Mech.*, **36**(6), 729-744.

Pandey, A.K., Kumar, R., Paul, D.K. and Trikha, D.N. (2006), "Strain rate model for dynamic analysis of reinforced concrete structures", *J. Struct. Eng.*, **132**(9), 1393-1401.

Rebora, B. and Zimmermann, Th. (1976), "Dynamic rupture analysis of reinforced concrete shells", *Nucl. Eng. Des.*, **37**(2), 269-297.

Sadique, M.R., Iqbal, M.A. and Bhargava, P. (2015), "Crash analysis of military aircraft on nuclear containment", *Struct. Eng. Mech.*, **53**(1), 73-87.

Sayed, M.A, Go, S., Cho S.G. and Kim, D. (2015), "Seismic responses of base isolated nuclear power plant structures considering spatially varying ground motions", *Struct. Eng. Mech.*, **54**(1), 169-188.

Schenk, O. and Gartner, K. (2004), "Solving unsymmetric sparse systems of linear equations with PARDISO", *J. Future Gener. Comput. Syst.*, **20**(3), 475-487.

Tamayo, J.L.P. (2015), "Numerical simulation of soil-pile interaction by using the finite element method", Ph.D. Dissertation, Federal University of Rio Grande do Sul, Porto Alegre.

Tamayo, J.L.P., Awruch, A.M. and Morsch, I.B. (2013b), "Numerical modeling of reinforced concrete structures: static and dynamic analysis", *Revista Escola de Minas*, **66**(4), 425-430.

Tamayo, J.L.P., Morsch, I.B. and Awruch, A.M. (2013a), "Static and dynamic analysis of reinforced concrete shells", *Latin Am. J. Solid. Struct.*, **10**(6), 1109-1134.

CC